JACS
JOURNAL OF THE AMERICAN CHEMICAL SOCIETY
pubs.acs.org/JACS
Article

[2 + 2] Cycloaddition Produces Divalent Organic Color-Centers with Reduced Heterogeneity in Single-Walled Carbon Nanotubes

Haoran Qu, Yulun Han, Jacob Fortner, Xiaojian Wu, Svetlana Kilina, Dmitri Kilin, Sergei Tretiak, and YuHuang Wang*

Cite This: J. Am. Chem. Soc. 2024, 146, 23582−23590
Read Online
ACCESS | Metrics & More | Article Recommendations | Supporting Information

ABSTRACT: Organic color centers (OCCs), generated by the covalent functionalization of single-walled carbon nanotubes, have been exploited for chemical sensing, bioimaging, and quantum technologies. However, monovalent OCCs can assume at least 6 different bonding configurations on the sp^2 carbon lattice of a chiral nanotube, resulting in heterogeneous OCC photoluminescence emissions. Herein, we show that a heat-activated [2 + 2] cycloaddition reaction enables the synthesis of divalent OCCs with a reduced number of atomic bonding configurations. The chemistry occurs by simply mixing enophile molecules (e.g., methylmaleimide, maleic anhydride, and 4-cyclopentene-1,3-dione) with an ethylene glycol suspension of SWCNTs at elevated temperature (70−140 °C). Unlike monovalent OCC chemistries, we observe just three OCC emission peaks that can be assigned to the three possible bonding configurations of the divalent OCCs based on density functional theory calculations. Notably, these OCC photoluminescence peaks can be controlled by temperature to decrease the emission heterogeneity even further. This divalent chemistry provides a scalable way to synthesize OCCs with tightly controlled emissions for emerging applications.

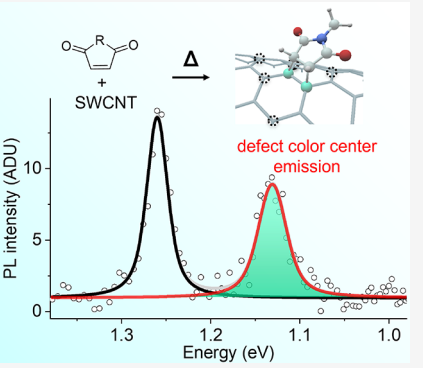

INTRODUCTION

Organic color centers (OCCs) are molecularly tunable quantum defects that can be synthesized by covalently attaching functional groups to the sidewalls of single-walled carbon nanotubes (SWCNTs).[1−4] These defects display many intriguing properties, including the formation of new optically allowed emission states (E_{11}^- and E_{11}^-*) that are red-shifted from the SWCNT band-edge emission (E_{11}) in the shortwave infrared.[1,3] These states have shown several unique properties including brightening dark excitons,[1] ultrafast trapping of excitons,[5] stabilization of trions,[6,7] and the emission of single photons at room temperature.[8] However, the majority of synthetic chemistries for OCCs (e.g., diazonium chemistry,[1,9,10] diazoether chemistry,[11] reductive alkylation,[2,12,13] and photoactivated radical addition[14−16]) are monovalent-based, which produce a large number of different, coexisting bonding configurations on the same nanotube structure.[17−19] This structural heterogeneity is in part due to the addition reaction to the nanotube double bond, which produces an unpaired electron that typically bonds with a H or OH group available in solution to close the valence state,[20] with the reaction occurring at any one of the six neighboring carbon atoms relative to the initial functional group (Figure 1a). This structural heterogeneity can be beneficial to certain applications, such as machine learning, which may require a large number of diverse structures, but in general, it has posed a synthetic challenge for emerging applications of OCCs in chemical sensing,[21−24] bioimaging,[25−27] disease diagnostics,[28,29] and as single photon sources.[8,30]

One possible solution to this heterogeneity problem is the use of divalent OCC functional groups in which the two bonds are created equally to the nanotube sidewall. However, currently available divalent OCCs (e.g., synthesized using 1,2-diiodobenezene) are produced as a mixture of both monovalent and divalent OCCs presumably due to the stepwise nature of the addition reaction.[12,14,31] An alternative divalent chemistry is cycloaddition, in which the two bonds are created simultaneously, and the divalent functional group provides its own pairing bond, which may help decrease the structural heterogeneity caused by the bonding of a different functional group.[12,32,33] One such cycloaddition chemistry is the Diels−Alder reaction, which typically features [4 + 2] cycloaddition between a diene and dienophile.[34−37] Star et al. have shown that cycloaddition reactions can proceed via a [2 + 2] pathway between enones and SWCNTs.[38] Conceptually, a cycloaddition reaction on SWCNTs would reduce the number of possible OCC bonding configurations to just 3−a

Received: June 17, 2024
Revised: July 30, 2024
Accepted: July 31, 2024
Published: August 5, 2024

https://doi.org/10.1021/jacs.4c08105
J. Am. Chem. Soc. 2024, 146, 23582−23590

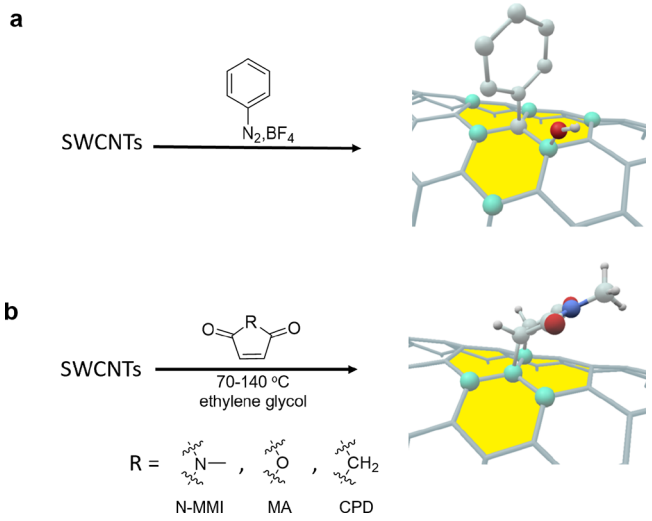

Figure 1. Schematic comparing monovalent vs [2 + 2] cycloaddition divalent OCCs and the resulting bonding configurations. (a) Monovalent chemistry using diazonium salt to functionalize SWCNTs. Six possible bonding configurations of the resulting OCCs are generated via an addition reaction on the sp^2 carbon lattice. The gray atom at the center shows the aryl group attachment site, while the pairing group (H or OH) may add to the other 6 atoms shown in cyan. (b) Divalent chemistry via [2 + 2] cycloaddition can be used to functionalize SWCNTs with enophile molecules, including N-MMI, MA, or CPD in ethylene glycol at elevated temperatures, producing 3 possible bonding configurations (shown in cyan atoms).

substantial reduction compared to the 6 bonding configurations of monovalent OCCs (Figure 1a,b). Furthermore, it is reasonable to suspect that the rotational constraint of divalent OCCs compared to their monovalent counterparts[39] may further reduce the emission line width. However, these important hypotheses have not been experimentally verified.

In this study, we demonstrate the synthesis of divalent OCCs with reduced structural heterogeneity on SWCNTs via [2 + 2] cycloaddition using enophiles such as methylmaleimide (N-MMI), maleic anhydride (MA), and 4-cyclopentene-1,3-dione (CPD). In the functionalized (6,5)-SWCNTs, we observed three distinct OCC photoluminescence (PL) peaks centered at 1112 (1.115 ± 0.008 eV), 1139 (1.089 ± 0.006 eV), and 1213 nm (1.022 ± 0.012 eV), whose predominance can be controlled by the reaction temperature. At lower temperatures (80 °C), the ∼1139 nm peak is favorably synthesized, while at 120 °C, the 1112 nm peak dominates. These observations are corroborated by density functional theory (DFT) calculations, providing evidence that [2 + 2] cycloaddition can reduce the atomic bonding configurations to just 3 on a chiral nanotube.

EXPERIMENTAL SECTION

Synthesis of OCCs through [2 + 2] Cycloaddition. The OCCs were synthesized using a [2 + 2] cycloaddition reaction involving the addition of various enophiles to the conjugated double-bond structure of SWCNTs. For a typical reaction, approximately 1−5 mg of SWCNT powder (CoMoCat SG65i, Sigma-Aldrich, lot no. MKBZ1159 V) was added to 5 mL of ethylene glycol (VWR, lot 000238286) in a 10 mL round-bottom flask. Next, 2−15 mg of an enophile (EP), such as methylmaleimide (N-MMI; Sigma-Aldrich, 97%), maleic anhydride (MA; Sigma-Aldrich, 99%), or 4-cyclopentene-1,3-dione (CPD; Sigma-Aldrich, 95%), was added to the mixture. The mole ratio of [EP]:[C] was in the range of 20:1−7:1, where [C] was based on the total mass of the SWCNT powder, irrespective of the (6,5)-SWCNT purity. The round-bottom flask was placed in a mineral oil bath and heated overnight at controlled temperatures between 70 and 140 °C. The mixture was continuously stirred with a stirring bar throughout the reaction. The reaction was stopped by cooling the mixture to room temperature. The SWCNTs were filtered out using a polyvinylidene fluoride membrane (MilliporeSigma VVLP membrane, 0.1 μm pore size) and rinsed with approximately 50 mL of nanopure water at least three times. The functionalized SWCNT material was then rinsed with 5 mL of ethanol at least three times to remove the remaining water. Finally, the powder was dried under a vacuum at room temperature for 1 h to obtain a dry powder of the OCC-functionalized SWCNTs (OCC-SWCNTs).

Individual Dispersion of OCC-SWCNTs. The dry OCC-SWCNT powder was dispersed by ultrasonication (Misonix 4000) in 1 wt/vol % sodium deoxycholate (DOC; Sigma-Aldrich)-H_2O solution at 4 W/mL for 30 min. Typically, approximately 1 mg of OCC-SWCNTs was dispersed by 1.5−2 mL of 1 wt/vol % DOC solution, followed by centrifugation at 25000*g* (1717 rad/s, 16400 rpm on Eppendorf centrifuge 5417 R) for 1 h to remove bundled SWCNTs.

PL Characterization. Ensemble PL spectra of the OCC-SWCNTs were collected by using a NanoLog spectrofluorometer (Horiba Jobin Yvon). The samples were excited with a 450 W xenon source dispersed by a double-grating monochromator. The slit width bandpass of the excitation and emission beams was both set to 10 nm. The PL spectra were collected using a liquid-N_2 cooled linear InGaAs array detector. The emission spectra were collected with excitation light at the E_{22} wavelength of each specific chirality. The integration time for the PL spectra and PL excitation map were 2−60 and 5 s, respectively. All samples were diluted with 1 wt % DOC and had an optical density at the E_{11} band of less than 0.5 (A/cm), measured using a PerkinElmer Lambda 1050 spectrophotometer with a broadband InGaAs detector.

PL images of the OCC-SWCNTs were imaged on the single nanotube level using a hyperspectral imaging setup.[40,41] In brief, ∼5 μL of the 1000-fold diluted OCC-SWCNTs solution was drop-cast on a polystyrene-coated Au-on-Si substrate. The polystyrene layer insulates the SWCNTs from contacting the Au, which would quench the PL, while the Au layer is used as a mirror to enhance the excitation and collection efficiency of the emission. An infrared optimized 100× objective (LCPLN100XIR, numerical aperture (NA) = 0.85, Olympus) was used, along with a continuous wave laser at 730 nm (Shanghai Dream Lasers Technology Co., Ltd.) as the excitation light source. Fluorescence emission from the sample was filtered through a long pass dichroic mirror (875 nm edge, Semrock, USA), which removed the elastic laser scattering from the sample and then dispersed by a volume Bragg grating (VBG; Photon Etc, Inc. Montreal, Canada). Only diffracted light with a narrow bandwidth of 3.7 nm was collected on the detector to form a spectral image.

As the functionalized SWCNT samples were prepared in ethylene glycol and sonicated under aqueous conditions, some peak position variation can be attributed to different degrees of water or ethylene glycol filling inside the nanotubes.[41−43] Therefore, a more accurate way to compare the relative energy of each bonding configuration is through the relative energy difference between the E_{11} peak and the OCC emission ($\Delta E = \Delta E = E_{\mathrm{OCC\ emission}} - E_{11}$), which corresponds to the OCC trapping depth.[44] Consequently, we deconvoluted the OCC emission peaks based on ΔE rather than solely using the emission energies.

Raman spectroscopy was performed by using a LabRAM ARAMIS Raman microscope (Horiba Jobin Yvon) with a 532 nm laser excitation (46 mW) and a 1.0 neutral density filter to prevent sample damage. The integration time was 1 s and repeated 10 times. The dispersed nanotube solution was precipitated with ethanol and then deposited on a Si substrate, whose 520.7 cm^{-1} Si peak served as a reference during the measurement.

Quantum-Chemical Modeling. All calculations except for transition state search and ab initio molecular dynamics (AIMD) were performed with Gaussian 09 software.[45] A 10 nm (6,5)-SWCNT

https://doi.org/10.1021/jacs.4c08105
J. Am. Chem. Soc. 2024, 146, 23582−23590

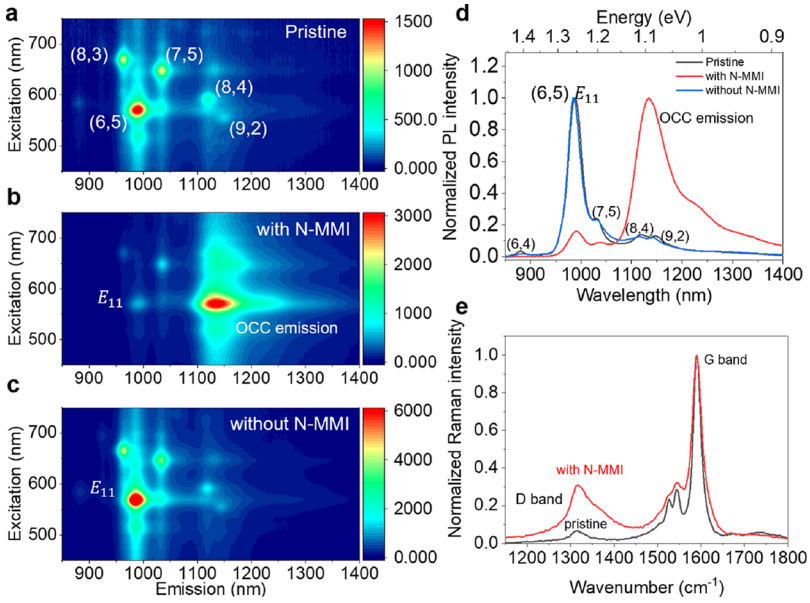

Figure 2. OCC generation on SWCNTs via cycloaddition using N-MMI. (a) PL excitation map of the pristine SWCNT starting material, which primarily features the (6, 5) nanotube chirality, but also contains other chiralities, including (8, 3), (7, 5), (8, 4), and (9, 2). (b) PL excitation−emission map of the nanotubes from (a) after reacting with N-MMI at a [N-MMI]:[C] ratio of 7:1 at 100 °C, showing the OCC emission at wavelengths in the range of 1100−1300 nm. (c) PL excitation map of the SWCNTs from (a) treated under the same conditions as in (b) at 100 °C, but without the addition of N-MMI. (d) PL spectra extracted from a-c of the pristine (6,5)-SWCNT starting material (black) after reaction with N-MMI at 100 °C (red) and after treatment with the same reaction conditions but without the addition of N-MMI (blue). The SWCNTs are excited at the E_{22} transition (565 nm). All the PL spectra were measured after dispersing the samples in 1 wt/vol % DOC/D_2O. Note that the small peaks in the pristine material and the "without N-MMI" control are the E_{11} or phonon sideband emissions from other nanotube chiralities. (e) Raman spectra of SWCNTs reacted with N-MMI (red) and the pristine SWCNT starting material (black). Note that the PL spectra are normalized to the maximum peak intensity and the Raman spectra are normalized to the G-band at ∼1590 cm^{-1}.

was functionalized with N-MMI at 3 positions (PP(1/3,1/3), PP(1/3,-2/3), and PP(−2/3,1/3)). The geometries of all structures were optimized using the Coulomb-attenuated B3LYP (CAM-B3LYP) functional[46] and 3-21G basis set.[47] The optical transitions were computed by using TD-DFT with the same functional and basis set. We analyzed the natural transition orbitals (NTOs)[48] with Gaussian 09 software and confirmed that the NTOs are strongly localized at the OCC, further verifying the defect origin of the optical transitions. We note that the simulated peaks are higher in energy compared to the experimental data mainly due to the finite length of the SWCNTs, the functional, the limited basis set, and the vacuum environment used in the simulations. However, these limitations do not change the relative emission energy ordering of the different bonding configurations[49] and hence we did not attempt to make corrections of the simulated peaks to the experimentally observed range as the correction is a qualitative adjustment and requires significantly more computational expense.

Transition State Search and AIMD. To better understand the reaction pathways, we applied the climbing-image nudged elastic band (CI-NEB)[50,51] and AIMD calculations. DFT calculations were carried out using the Vienna ab initio simulation package (VASP)[52] with the generalized gradient approximation (GGA) Perdew−Burke−Ernzerhof (PBE)[53] functional in a plane-wave basis set along with projector augmented-wave (PAW) pseudopotentials.[54] For geometry optimization, we used a plane-wave cutoff of 400 eV and optimized the atomistic models until the total energy converged to a threshold of 1 × 10^{-6} eV. We generated (6,5) SWCNTs with one unit cell (364 atoms) and extended the length along the tubular axis to infinity under periodic boundary conditions. Vacuum spacings of 9 Å were added in the x and y directions to minimize spurious interactions. The overall size of the rectangular simulation cell was 26.26, 16.50, and 40.68 Å. The CI-NEB calculations were carried out with a force tolerance of 0.01 eV/Å. For AIMD calculations, the PP(1/3, 1/3) configuration was first heated to 300 K for a duration of 150 fs with a time step of 0.5 fs by a Nosé−Hoover thermostat with repeated velocity rescaling. Then, 1 ps microcanonical trajectories were generated using the Verlet algorithm with a time step of 1 fs. All calculations were performed at the Γ point.

RESULTS AND DISCUSSION

To synthesize the divalent OCCs via [2 + 2] cycloaddition, we used CoMoCat SG65i SWCNTs, which primarily consist of the (6,5) nanotube chirality, along with minor (8,3) and (7,5) components and a limited amount of larger diameter nanotubes, such as (9,2) and (8,4). Figure 2a shows a two-dimensional (2D) PL excitation−emission map of the SG65i starting material in which the E_{11} emissions of the different chiralities can be identified. To conduct the [2 + 2] cycloaddition reaction, 1−5 mg of this SWCNT powder was added to ethylene glycol, which is a highly viscous "solvent" that can kinetically suspend the SWCNTs (as bundles) by the shearing force created from a stir bar, in which the resulting suspension remains stable for ∼2 days. We added 2−15 mg of the enophile molecules, such as N-MMI, MA, or CPD, to this SWCNT suspension under stirring, and then heated the mixture overnight at different temperatures, ranging from 70 to 140 °C, to activate the reaction. The resulting OCC-functionalized SWCNTs (OCC-SWCNTs) were then subsequently dispersed in 1 wt/vol % sodium deoxycholate (DOC)/D_2O solution for further characterization (see the Experimental Section for details).

After the reaction, we measured the 2D excitation−emission map of the samples to determine whether or not the OCCs were successfully added to the nanotubes. Figure 2b shows the ensemble PL results of the N-MMI functionalized SWCNTs (N-MMI-SWCNTs) at 100 °C. Compared to the pristine starting material, the functionalized SWCNTs display multiple

https://doi.org/10.1021/jacs.4c08105
J. Am. Chem. Soc. 2024, 146, 23582−23590

OCC emissions[18] red-shifted from the E_{11} peaks of the individual chiralities, convoluted at >1100 nm. In contrast, when we treated the SWCNTs to the same reaction conditions but without adding N-MMI, we observed the same E_{11} SWCNT emission (Figure 2c) as that of the pristine nanotubes (Figure 2a). The PL emission spectra of the pristine SWCNTs, N-MMI-SWCNTs, and the control without the addition of N-MMI are shown in Figure 2d by using 565 nm excitation, which corresponds to the E_{22} band of the (6,5)-SWCNTs. For the SWCNTs reacted with N-MMI at 100 °C, there is a bright OCC emission peak (E_{11}^-) at ∼1130 nm (1.097 eV) with a shoulder band extending to 1400 nm (0.886 eV). In contrast, the control group (no N-MMI added) shows no significant increase in PL intensity in the range of >1100 nm, though its E_{11} emission shows a marginal blueshift of ∼1−2 nm compared to the pristine nanotubes. These control experiments exclude side reactions due to the solvent or dissolved oxygen. We also measured the 2D PL maps and emission spectra (565 nm excitation) for SWCNTs reacted with MA and CPD at 100 °C (Figure S1). Similar to N-MMI, new OCC-induced emission was observed for both samples in the range of 1100−1300 nm.

We measured the Raman spectra of the reacted samples to further confirm the covalent functionalization of the SWCNTs rather than surface adsorption. Figure 2e shows the Raman spectra of the pristine SWCNTs and N-MMI-SWCNTs. The Raman G-band (∼1590 cm^{-1}) is related to the stretching of the sp^2 C−C bonds in graphitic material. The Raman D-band, known as the disorder band or the defect band,[55] appears as a minor peak at ∼1316 cm^{-1} in the pristine sample. Upon covalent functionalization, the conversion of the sp^2 hybridized carbon atoms into sp^3 results in a noticeable increase in the Raman D-band in N-MMI-SWCNTs. Specifically, after the reaction, the D/G ratio increased from 0.07 to 0.31. Note that the starting nanotube material (SG65i) contains metallic nanotubes, which could react more efficiently than the semiconductors, and it is difficult to quantify their contributions. However, these results show that the OCCs are covalently created on the SWCNTs, which generates the optically allowed OCC PL emission in the observed red-shifted range.[9,18,40]

To further investigate the convoluted emission of the N-MMI-SWCNTs prepared at 100 °C (1100−1300 nm, Figure 2b), we utilized hyperspectral PL microscopy to directly observe the PL of individual nanotubes.[40] This method allows us to circumvent averaging effects in the ensemble PL to observe which individual E_{11}^- emissions may occur. To prepare the sample, we dispersed the nanotubes in 1 wt/vol % DOC aqueous solution, which we deposited on a polystyrene (PS)-coated Au on Si substrate (see the Experimental Section). Note that ultrasonication was used during the dispersion step, which cuts the SWCNTs short, beyond the diffraction limit.[56] Therefore, the individual nanotube PL appears as white spots rather than rodlike, as shown in Figure 3a. In addition to using tip sonication and centrifugation to individualize and remove nanotube bundles, the sample was diluted 1000-fold prior to deposition on the substrate to ensure the SWCNTs were well-separated and individualized.

Unlike the ensemble PL, which featured convoluted OCC emission, the hyperspectral imaging revealed 80 individual N-MMI-SWCNTs (Figure 3b) that featured three distinct OCC peaks. The average peak positions were centered at

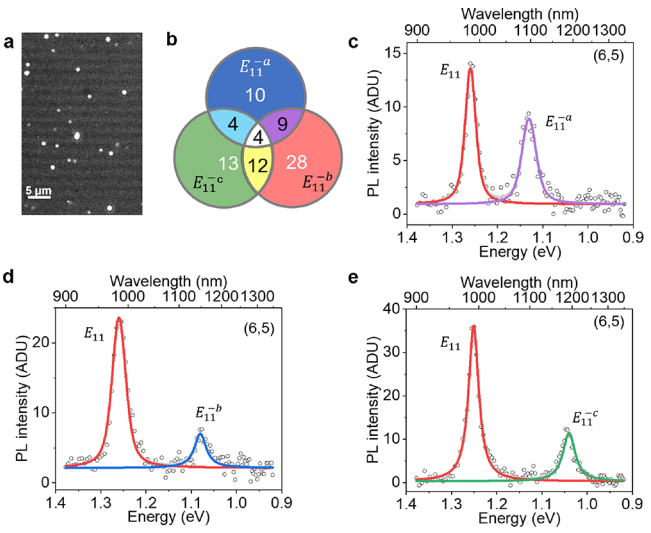

Figure 3. Hyperspectral PL imaging of individual (6,5)-SWCNTs-N-MMI. (a) Photoluminescence image of the N-MMI-SWCNTs taken in a broadband mode covering the 900−1550 nm hyperspectral range. (b) Venn diagram illustrating the statistically analyzed OCC functionalization emissions of the 80 measured individual nanotubes synthesized at 100 °C. Three sets of nanotubes are found: nanotubes containing E_{11}^{-a} only (blue), nanotubes containing E_{11}^{-b} only (red), and nanotubes containing E_{11}^{-c} only (green). The overlap between circles represents nanotubes containing two or more of the OCC emission peaks. The numbers indicate the number of nanotubes containing one or more specific OCC peaks. (c−e) PL spectra of individual (6,5)-SWCNTs-N-MMI with different OCC emission peaks of (c) E_{11}^{-a} at 1112 nm (1.115 eV), (d) E_{11}^{-b} at 1139 nm (1.089 eV), and (e) E_{11}^{-c} at 1213 nm (1.022 eV).

approximately 1117 (1.111 ± 0.008 eV), 1145 (1.083 ± 0.009 eV), and 1216 nm (1.019 ± 0.015 eV), as shown in Figure 3c−e. We denote these peaks as E_{11}^{-a}, E_{11}^{-b}, and E_{11}^{-c}, respectively, all of which feature a similar full width at half-maximum (fwhm) of 0.033 ± 0.007, 0.033 ± 0.006, and 0.038 ± 0.011 eV (Table S1). While some nanotubes displayed only one of these peaks, we also observed convoluted, multipeak OCC emission from individual nanotubes and built a histogram of the OCC emission peaks (Figure S2). Note that in these individual nanotubes, the E_{11}^- to E_{11} PL intensity ratio ranges from 1:3 to 1:2, suggesting a relatively low defect density. Similar OCC emissions were recorded for (8,3)- and (7,5)-SWCNTs functionalized by the same cycloaddition reaction using N-MMI (Figure S3).

These results suggest that the three observed OCC emission peaks may be related to the 3 possible bonding configurations of the [2 + 2] cycloaddition product, which is significantly reduced compared to the 6 distinct emission peaks of the six bonding configurations created by monovalent diazonium chemistry.[4,57] Additionally, we hypothesize that more than one OCC with different bonding configurations can be present on the same SWCNT, which would explain the multipeak emission observed from some of the individual nanotubes. We note that [2 + 2] cycloaddition reactions typically require photoactivation. The observation of thermally activated [2 + 2] reactions with SWCNTs was therefore surprising, which warrants further studies to explore the underlying mechanism.

To further explore these 3 different OCC emission peaks, we aimed to control the reaction products using temperature. First, we functionalized SWCNTs at different temperatures

https://doi.org/10.1021/jacs.4c08105
J. Am. Chem. Soc. 2024, 146, 23582−23590

ranging from 80 to 120 °C at a [N-MMI]:[C] ratio of 7:1 and measured the ensemble PL spectra (Figure 4) as well as the 2D

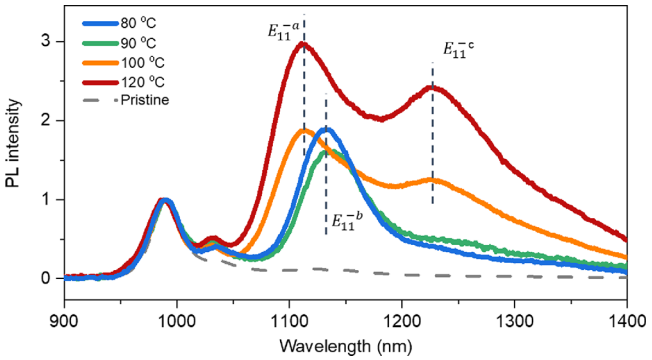

Figure 4. Temperature-dependent OCC emission from the reaction of (6,5)-SWCNTs with N-MMI at [N-MMI]:[C] = 7:1. PL spectra of (6,5)-SWCNTs reacted at 80 °C (blue), 90 °C (green), 100 °C (orange), and 120 °C (red). The PL spectrum of the pristine SWCNTs is shown by the dashed gray line. The PL spectra are normalized to the E_{11} emission of the (6,5)-SWCNTs.

PL maps (Figure S4). Note that we deconvoluted the OCC emissions in the ensemble PL spectra of these samples based on the relative energy difference between the E_{11} and E_{11}^{-} peaks (ΔE), as determined from the single nanotube hyperspectral imaging results (see Table S1 and the Experimental Section for details). At a reaction temperature of 80 °C, the resulting OCC emission primarily features E_{11}^{-b} at ∼1130 nm (∼1.097 eV) (Figure 4, Figure S4a). As we increase the temperature beyond 90 °C, E_{11}^{-c} and E_{11}^{-a} appear and ultimately begin to dominate the spectra. Specifically, at 120 °C, the OCC emission switches to E_{11}^{-a} at ∼1111 nm (∼1116 eV) along with E_{11}^{-c} at ∼1228 nm (1.010 eV) (Figure 4, Figure S4d). Similarly, we investigated the temperature dependence of the implantation of the OCC using MA ([MA]:[C] = 20:1) at reaction temperatures of 70 to 140 °C (Figure S5). The lower reaction temperature (70−90 °C) favors E_{11}^{-b}, while the higher temperature (110−140 °C) favors the formation of E_{11}^{-a}. E_{11}^{-c} is also generated at medium temperature (90−110 °C). However, at a higher temperature of 140 °C, E_{11}^{-c} is less favorable, and the main emission is E_{11}^{-a}. We note that the relative reactant ratios also affect the peak distribution (Figure S6), but this effect is less pronounced compared with the temperature. These results suggest that the formation of E_{11}^{-b} is kinetically favored with a smaller activation energy, while the formation of E_{11}^{-a} and E_{11}^{-c} requires a higher activation energy (Figure S7). However, E_{11}^{-a} is more favorably synthesized at higher temperatures compared to E_{11}^{-c}. Therefore, the E_{11}^{-a} emission likely derives from the most thermodynamically stable OCC product compared to E_{11}^{-b} and E_{11}^{-c}.

To gain an atomistic understanding of the three OCC emissions, we utilized first-principles simulations of the (6,5)-SWCNTs-N-MMI. A DFT framework was employed to explore the potential energy landscape and perform ab initio molecular dynamics (AIMD), while time-dependent DFT (TD-DFT) was used to calculate the optical properties, as described in the Experimental Section. As model systems, three bonding configurations of 10 nm-long (6,5)-SWCNTs were constructed with N-MMI OCCs via the [2 + 2] cycloaddition mechanism[37] at different pairing positions (PP) of PP(−2/3, 1/3), PP(1/3, 1/3), and PP(1/3, −2/3), as shown in Figure 5a−c. This notation of bonding configuration was adopted from our previous study.[18] For (6,5)-SWCNTs, these three PPs create 33, 87, and 27° angles with respect to the SWCNT axis, respectively.

Furthermore, the five-membered ring of the N-MMI is tilted on the helical surface of the (6,5)-SWCNT. DFT calculations on six different configurations using the PBE functional and a plane-wave basis set (Figure S8) showed that the tilt angle of the N-MMI group has a negligible impact on the ground and excited state properties. Instead, the most significant effect arises from the relative position of the functional group with

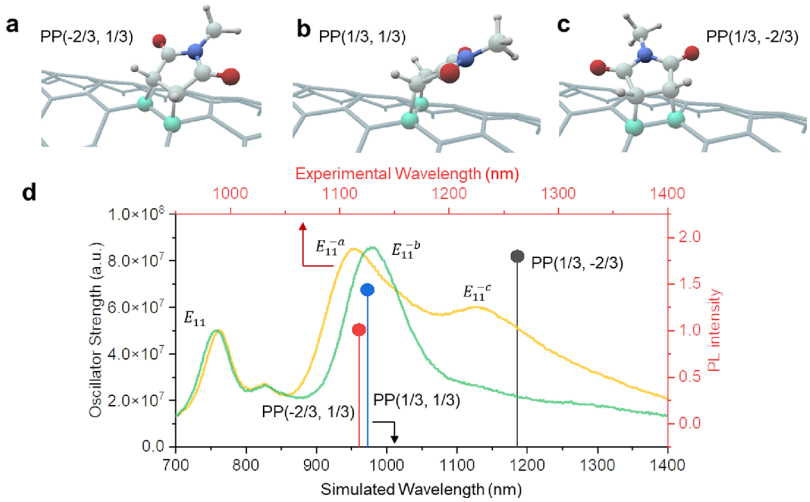

Figure 5. Emission and relative energy of the three possible bonding configurations of OCCs generated by N-MMI. (a−c) Schematics of the OCC bonding configurations formed on the SWCNT based on the [2 + 2] cycloaddition reaction, in which the functional group is covalently bonded at a pair of nanotube carbon atoms indicated by (a) PP(−2/3, 1/3) (33° to the SWCNT axis), (b) PP(1/3, 1/3) (87° to the SWCNT axis), and (c) PP(1/3, −2/3) (27° to the SWCNT axis). (d) TD-DFT simulated emission wavelengths of OCCs featuring the PP(−2/3, 1/3) (red), PP(1/3, 1/3) (blue), and PP(1/3, −2/3) (black) bonding configurations (oscillator strength vs simulated wavelength shown in the left and bottom axes in black), superimposed with the experimental PL spectra from (6,5)-SWCNTs-N-MMI synthesized at 80 (green) and 100 °C (yellow) (PL intensity vs experimental wavelength shown in the right and top axes in red).

https://doi.org/10.1021/jacs.4c08105
J. Am. Chem. Soc. 2024, 146, 23582−23590

respect to the nanotube's axis (Tables S2 and S3). Based on the geometry optimization, we obtained the total energies of each isomer relative to PP(−2/3, 1/3), which has the lowest total energy (Table S4). The other two isomers were 0.100 and 0.069 eV higher than that of PP(−2/3, 1/3), suggesting that they are kinetic products.

We next simulated the excited states of these isomers via TD-DFT to obtain the OCC PL wavelengths of each isomer. Figure 5d and Table S5 show that PP(−2/3, 1/3), PP(1/3, 1/3), and PP(1/3,-2/3) have simulated OCC emissions at 960, 972, and 1186 nm, respectively. These divalent attachments result in significantly less distortion of structural symmetry compared with monovalent defects. Specifically, the PP(−2/3, 1/3) and PP(1/3, 1/3) defects exhibit nearly identical angles (29.5° and 30.5°) relative to the chiral vector of the (6,5) SWCNT. This reduced distortion leads to nearly degenerate excitons associated with these defects. Similar findings have been predicted for other types of divalent OCCs,[33] suggesting a general trend of lower spectral diversity for divalent defects compared to their monovalent counterparts. It is important to note that the wavelengths obtained with TD-DFT are blue-shifted compared to what is observed experimentally due to the limitation of the computational methodology. The approximations include quantum confinement effects due to the vacuum environment and the short tube length used in the model as well as the limited basis set.[39] Since these factors affect the emission signal for all model systems similarly and do not change the relative energy ordering between the different bonding configurations,[49] the relative positions of the three peaks allow for a reasonable assignment of the experimental peaks. As shown in Figure 5d, comparing the simulated peaks to the experimental data allows us to assign the thermodynamic bonding configuration PP(−2/3, 1/3) to the E_{11}^{-a} peak at 1112 nm, while the kinetic configurations of PP(1/3, 1/3) and PP(1/3, −2/3) can be assigned to E_{11}^{-b} at 1139 nm and E_{11}^{-c} at 1213 nm, respectively. We further constructed the natural transition orbitals of these OCCs, which support these excited state assignments (Figure S9). The results consistently suggest that the [2 + 2] cycloaddition chemistry can effectively reduce the number of possible bonding sites.

We further evaluated the reaction pathways for the three bonding configurations using the climbing image extension of the nudged elastic band (CI-NEB) approach (Experimental Section). Here, the initial reactants were generated by shifting the functional groups of corresponding bonding configurations about 3.7 Å along the Z axis. Although these initial reactants are not identical, the energy variation is minimal (∼0.007 eV). Along the reaction pathways, we find 10 intermediate structures, with the highest energy structure corresponding to the saddle point, i.e., the transition state (Figure 6 top panel). Throughout all pathways, it is found that the N-MMI gradually approaches the tube. At the transition state, the C═C bond in the N-MMI molecule elongates from ∼1.3 to 1.5 Å, and a C−C bond of ∼1.6 Å forms between the molecule and the tube. In later stages, a second C−C bond forms, leading to a four-membered ring with bond lengths of ∼1.6 Å. Our calculations reveal that the three bonding configurations exhibit different barrier heights (Figure 6 bottom panel). The thermodynamically stable structure PP(−2/3, 1/3) has the lowest barrier of 2.17 eV, while the kinetic configurations of PP(1/3, 1/3) and PP(1/3, −2/3) have slightly higher barriers of 2.35 and 2.20 eV, respectively. Note that these calculations are carried out in vacuum conditions, a significant

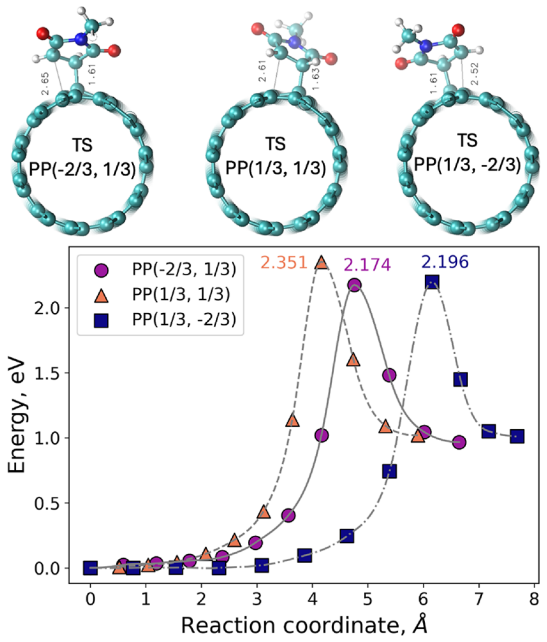

Figure 6. Transition state search by the CI-NEB method shows that the cycloaddition reaction pathways of the three divalent OCCs on (6,5)-SWCNT are similar, with differences in barrier heights, suggesting kinetic control of divalent OCCs using temperature. The top panels show the calculated three transition states, whereas the bottom panel depicts the potential energy along the reaction coordinate.

approximation compared to experimental measurements performed in solvent environments. Therefore, the absolute values of the barrier heights are not quantitative. Nonetheless, the variations in barrier heights align with our expectations about the temperature dependence of product distributions. Finally, we expect the presence of complex chemical dynamics mediated by thermal fluctuations toward the formation of thermodynamically stable products. To illustrate this possibility, we conducted AIMD simulations of the PP(1/3, 1/3) configuration under ambient conditions. A sample trajectory shown in Figure S10 shows the formation of a more stable configuration concomitant to the elongating C−C bond within the four-membered ring structure on the tube. A detailed theoretical investigation of these dynamics will be presented in our follow-up study.

CONCLUSIONS

We demonstrate that the addition of enophile molecules to SWCNTs can enable a [2 + 2] cycloaddition reaction to produce divalent OCCs with just three bonding configurations on chiral nanotubes. These three bonding configurations can be controlled by the reaction temperature. A low temperature (70−90 °C) favors the synthesis of the E_{11}^{-b} OCC bonding configuration emitting at 1139 nm, which is likely a kinetically favored product. A higher temperature (110−120 °C) favors the synthesis of E_{11}^{-a} and E_{11}^{-c} sites emitting at 1112 and 1213 nm. The synthesis of E_{11}^{-c} becomes suppressed at an even higher temperature of 140 °C. The relative system energy and the OCC emission wavelengths were rationalized by first-principles simulations, which we used to assign the OCC emissions to the three distinct bonding configurations. Our results suggest that the E_{11}^{-b} and E_{11}^{-c} emissions are related to kinetic OCC products, while E_{11}^{-a} corresponds to the

https://doi.org/10.1021/jacs.4c08105
J. Am. Chem. Soc. 2024, 146, 23582−23590

thermodynamically most stable bonding configuration. These findings demonstrate a potentially scalable method that can be used for various SWCNT chiralities to create structurally controlled chiral OCCs at specific bonding configurations. Importantly, this cycloaddition reaction does not require a catalyst, nor does it generate byproducts[34] that can affect the nanotube emission properties. These findings help address the heterogeneity challenge and provide a scalable synthesis of OCCs for applications that require narrow emission.[3,8,30]

■ ASSOCIATED CONTENT

Supporting Information

The Supporting Information is available free of charge at https://pubs.acs.org/doi/10.1021/jacs.4c08105.

Excitation−emission photoluminescence maps, PL spectra of individual N-MMI-(6,5)-SWCNTs, temperature dependence of reactions involving N-MMI and MA, reagent concentration dependence, optimized geometries and energy of defects and their tilted counterparts, natural transition orbitals of OCCs, and AIMD trajectory (PDF)

■ AUTHOR INFORMATION

Corresponding Author

YuHuang Wang − *Department of Chemistry and Biochemistry, Chemical Physics Program, and Maryland NanoCenter, University of Maryland, College Park, Maryland 20742, United States;* orcid.org/0000-0002-5664-1849; Email: yhw@umd.edu

Authors

Haoran Qu − *Department of Chemistry and Biochemistry, University of Maryland, College Park, Maryland 20742, United States;* orcid.org/0000-0003-4536-6703

Yulun Han − *Department of Chemistry and Biochemistry, North Dakota State University, Fargo, North Dakota 58102, United States;* orcid.org/0000-0002-8619-0233

Jacob Fortner − *Chemical Physics Program, University of Maryland, College Park, Maryland 20742, United States*

Xiaojian Wu − *Department of Chemistry and Biochemistry, University of Maryland, College Park, Maryland 20742, United States*

Svetlana Kilina − *Department of Chemistry and Biochemistry, North Dakota State University, Fargo, North Dakota 58102, United States;* orcid.org/0000-0003-1350-2790

Dmitri Kilin − *Department of Chemistry and Biochemistry, North Dakota State University, Fargo, North Dakota 58102, United States;* orcid.org/0000-0001-7847-5549

Sergei Tretiak − *Center for Nonlinear Studies, and Theoretical Division, Los Alamos National Laboratory, Los Alamos, New Mexico 87545, United States;* orcid.org/0000-0001-5547-3647

Complete contact information is available at: https://pubs.acs.org/10.1021/jacs.4c08105

Notes

The authors declare no competing financial interest.

■ ACKNOWLEDGMENTS

This work is supported in part by the National Science Foundation (grant no. CHE2204202). We also gratefully acknowledge the NIH/National Institute of Biomedical Imaging and Bioengineering (grant no. R01EB033651) for partial support. SK and DK acknowledge the financial support from the DOE EPSCoR program: Building EPSCoR-State/National Laboratory Partnerships (grant number: DE-SC0021287) for computational research focused on the adaptation and application of photoexcited dynamics to functionalized carbon nanotubes. D.K. also thanks the NSF CAREER program (grant number: 1944921) for supporting the development of computational methods for simulating photoreactions and excited state dynamics. We thank the University of Maryland supercomputing resources made available for conducting the TD-DFT calculations. For computational resources used for simulations of photoexcited dynamics, we thank the Center for Computationally Assisted Science and Technology (CCAST) at North Dakota State University, which received partial enhancement through the DOE grant no. DE-SC0022239, and the National Energy Research Scientific Computing Center (NERSC), supported by the Office of Science of the DOE under Contract Number DE-AC02-05CH11231. The work at Los Alamos National Laboratory was performed in part at the Center for Integrated Nanotechnologies (CINT), a U.S. Department of Energy, Office of Science User Facility. Part of this work was adapted from Qu, H. (2022). *Fluorescent Carbon Nanotubes as Molecular Sensors and Color-Center Hosts* (dissertation, University of Maryland, College Park).

■ REFERENCES

(1) Piao, Y.; Meany, B.; Powell, L. R.; Valley, N.; Kwon, H.; Schatz, G. C.; Wang, Y. Brightening of carbon nanotube photoluminescence through the incorporation of sp3 defects. *Nat. Chem.* **2013**, *5*, 840−845.

(2) Shiraki, T.; Miyauchi, Y.; Matsuda, K.; Nakashima, N. Carbon Nanotube Photoluminescence Modulation by Local Chemical and Supramolecular Chemical Functionalization. *Acc. Chem. Res.* **2020**, *53*, 1846−1859.

(3) Brozena, A. H.; Kim, M.; Powell, L. R.; Wang, Y. Controlling the optical properties of carbon nanotubes with organic colour-centre quantum defects. *Nat. Rev. Chem.* **2019**, *3*, 375−392.

(4) Gifford, B. J.; Kilina, S.; Htoon, H.; Doorn, S. K.; Tretiak, S. Controlling Defect-State Photophysics in Covalently Functionalized Single-Walled Carbon Nanotubes. *Acc. Chem. Res.* **2020**, *53*, 1791−1801.

(5) Sykes, M. E.; Kim, M.; Wu, X.; Wiederrecht, G. P.; Peng, L.; Wang, Y.; Gosztola, D. J.; Ma, X. Ultrafast Exciton Trapping at sp3 Quantum Defects in Carbon Nanotubes. *ACS Nano* **2019**, *13*, 13264−13270.

(6) Brozena, A. H.; Leeds, J. D.; Zhang, Y.; Fourkas, J. T.; Wang, Y. Controlled defects in semiconducting carbon nanotubes promote efficient generation and luminescence of trions. *ACS Nano* **2014**, *8*, 4239−4247.

(7) Kwon, H.; Kim, M.; Nutz, M.; Hartmann, N. F.; Perrin, V.; Meany, B.; Hofmann, M. S.; Clark, C. W.; Htoon, H.; Doorn, S. K.; Hogele, A.; Wang, Y. Probing Trions at Chemically Tailored Trapping Defects. *ACS Cent. Sci.* **2019**, *5*, 1786−1794.

(8) He, X.; Hartmann, N. F.; Ma, X.; Kim, Y.; Ihly, R.; Blackburn, J. L.; Gao, W.; Kono, J.; Yomogida, Y.; Hirano, A.; Tanaka, T.; Kataura, H.; Htoon, H.; Doorn, S. K. Tunable room-temperature single-photon emission at telecom wavelengths from sp3 defects in carbon nanotubes. *Nat. Photonics* **2017**, *11*, 577−582.

(9) Luo, H. B.; Wang, P.; Wu, X.; Qu, H.; Ren, X.; Wang, Y. One-Pot, Large-Scale Synthesis of Organic Color Center-Tailored Semiconducting Carbon Nanotubes. *ACS Nano* **2019**, *13*, 8417−8424.

(10) Berger, F. J.; Lüttgens, J.; Nowack, T.; Kutsch, T.; Lindenthal, S.; Kistner, L.; Müller, C. C.; Bongartz, L. M.; Lumsargis, V. A.;

Zakharko, Y.; Zaumseil, J. Brightening of Long, Polymer-Wrapped Carbon Nanotubes by sp3 Functionalization in Organic Solvents. *ACS Nano* **2019**, *13*, 9259−9269.
(11) Powell, L. R.; Kim, M.; Wang, Y. Chirality-Selective Functionalization of Semiconducting Carbon Nanotubes with a Reactivity-Switchable Molecule. *J. Am. Chem. Soc.* **2017**, *139*, 12533−12540.
(12) Kwon, H.; Furmanchuk, A.; Kim, M.; Meany, B.; Guo, Y.; Schatz, G. C.; Wang, Y. Molecularly Tunable Fluorescent Quantum Defects. *J. Am. Chem. Soc.* **2016**, *138*, 6878−6885.
(13) Zhang, Y.; Valley, N.; Brozena, A. H.; Piao, Y.; Song, X.; Schatz, G. C.; Wang, Y. Propagative Sidewall Alkylcarboxylation that Induces Red-Shifted Near-IR Photoluminescence in Single-Walled Carbon Nanotubes. *J. Phys. Chem. Lett.* **2013**, *4*, 826−830.
(14) Wu, X.; Kim, M.; Kwon, H.; Wang, Y. Photochemical Creation of Fluorescent Quantum Defects in Semiconducting Carbon Nanotube Hosts. *Angew. Chem., Int. Ed. Engl.* **2018**, *57*, 648−653.
(15) Kozawa, D.; Wu, X.; Ishii, A.; Fortner, J.; Otsuka, K.; Xiang, R.; Inoue, T.; Maruyama, S.; Wang, Y.; Kato, Y. K. Formation of organic color centers in air-suspended carbon nanotubes using vapor-phase reaction. *Nat. Commun.* **2022**, *13*, 2814.
(16) Wu, X.; Kim, M.; Wang, L. J.; Veetil, A. K.; Wang, Y. Programming sp3 Quantum Defects along Carbon Nanotubes with Halogenated DNA. *J. Am. Chem. Soc.* **2024**, *146*, 8826−8831.
(17) Saha, A.; Gifford, B. J.; He, X.; Ao, G.; Zheng, M.; Kataura, H.; Htoon, H.; Kilina, S.; Tretiak, S.; Doorn, S. K. Narrow-band single-photon emission through selective aryl functionalization of zigzag carbon nanotubes. *Nat. Chem.* **2018**, *10*, 1089−1095.
(18) Qu, H.; Wu, X.; Fortner, J.; Kim, M.; Wang, P.; Wang, Y. Reconfiguring Organic Color Centers on the sp2 Carbon Lattice of Single-Walled Carbon Nanotubes. *ACS Nano* **2022**, *16*, 2077−2087.
(19) Settele, S.; Berger, F. J.; Lindenthal, S.; Zhao, S.; El Yumin, A. A.; Zorn, N. F.; Asyuda, A.; Zharnikov, M.; Högele, A.; Zaumseil, J. Synthetic control over the binding configuration of luminescent sp3-defects in single-walled carbon nanotubes. *Nat. Commun.* **2021**, *12*, 2119.
(20) Schmidt, G.; Gallon, S.; Esnouf, S.; Bourgoin, J.; Chenevier, P. Mechanism of the coupling of diazonium to single-walled carbon nanotubes and its consequences. *Chem. - Eur. J.* **2009**, *15*, 2101−2110.
(21) Kwon, H.; Kim, M.; Meany, B.; Piao, Y.; Powell, L. R.; Wang, Y. Optical Probing of Local pH and Temperature in Complex Fluids with Covalently Functionalized, Semiconducting Carbon Nanotubes. *J. Phys. Chem. C* **2015**, *119*, 3733−3739.
(22) Shiraki, T.; Onitsuka, H.; Shiraishi, T.; Nakashima, N. Near infrared photoluminescence modulation of single-walled carbon nanotubes based on a molecular recognition approach. *Chem. Commun.* **2016**, *52*, 12972−12975.
(23) Mann, F. A.; Herrmann, N.; Opazo, F.; Kruss, S. Quantum Defects as a Toolbox for the Covalent Functionalization of Carbon Nanotubes with Peptides and Proteins. *Angew. Chem., Int. Ed. Engl.* **2020**, *59*, 17732−17738.
(24) Kim, M.; McCann, J. J.; Fortner, J.; Randall, E.; Chen, C.; Chen, Y.; Yaari, Z.; Wang, Y.; Koder, R. L.; Heller, D. A. Quantum Defect Sensitization via Phase-Changing Supercharged Antibody Fragments. *J. Am. Chem. Soc.* **2024**, *146*, 12454−12462.
(25) Hong, G.; Diao, S.; Antaris, A. L.; Dai, H. Carbon Nanomaterials for Biological Imaging and Nanomedicinal Therapy. *Chem. Rev.* **2015**, *115*, 10816−10906.
(26) Jackson, C. T.; Jeong, S.; Dorlhiac, G. F.; Landry, M. P. Advances in engineering near-infrared luminescent materials. *iScience* **2021**, *24*, No. 102156.
(27) Mandal, A. K.; Wu, X.; Ferreira, J. S.; Kim, M.; Powell, L. R.; Kwon, H.; Groc, L.; Wang, Y.; Cognet, L. Fluorescent sp(3) Defect-Tailored Carbon Nanotubes Enable NIR-II Single Particle Imaging in Live Brain Slices at Ultra-Low Excitation Doses. *Sci. Rep.* **2020**, *10*, 5286.
(28) Kim, M.; Chen, C.; Wang, P.; Mulvey, J. J.; Yang, Y.; Wun, C.; Antman-Passig, M.; Luo, H.-B.; Cho, S.; Long-Roche, K.; Ramanathan, L. V.; Jagota, A.; Zheng, M.; Wang, Y.; Heller, D. A. Detection of ovarian cancer via the spectral fingerprinting of quantum-defect-modified carbon nanotubes in serum by machine learning. *Nat. Biomed. Eng.* **2022**, *6*, 267−275.
(29) Kim, M.; Chen, C.; Yaari, Z.; Frederiksen, R.; Randall, E.; Wollowitz, J.; Cupo, C.; Wu, X.; Shah, J.; Worroll, D.; Lagenbacher, R. E.; Goerzen, D.; Li, Y.-M.; An, H.; Wang, Y.; Heller, D. A. Nanosensor-based monitoring of autophagy-associated lysosomal acidification in vivo. *Nat. Chem. Biol.* **2023**, *19*, 1448−1457.
(30) Husel, L.; Trapp, J.; Scherzer, J.; Wu, X.; Wang, P.; Fortner, J.; Nutz, M.; Hümmer, T.; Polovnikov, B.; Förg, M.; Hunger, D.; Wang, Y.; Högele, A. Cavity-enhanced photon indistinguishability at room temperature and telecom wavelengths. *Nat. Commun.* **2024**, *15*, 3989.
(31) Hayashi, K.; Niidome, Y.; Shiga, T.; Yu, B.; Nakagawa, Y.; Janas, D.; Fujigaya, T.; Shiraki, T. Azide modification forming luminescent sp2 defects on single-walled carbon nanotubes for near-infrared defect photoluminescence. *Chem. Commun.* **2022**, *58*, 11422−11425.
(32) Wang, P.; Fortner, J.; Luo, H.; Kłos, J.; Wu, X.; Qu, H.; Chen, F.; Li, Y.; Wang, Y. Quantum Defects: What Pairs with the Aryl Group When Bonding to the sp2 Carbon Lattice of Single-Wall Carbon Nanotubes? *J. Am. Chem. Soc.* **2022**, *144*, 13234−13241.
(33) Gifford, B. J.; He, X.; Kim, M.; Kwon, H.; Saha, A.; Sifain, A. E.; Wang, Y.; Htoon, H.; Kilina, S.; Doorn, S. K.; Tretiak, S. Optical Effects of Divalent Functionalization of Carbon Nanotubes. *Chem. Mater.* **2019**, *31*, 6950−6961.
(34) Tobia, D.; Harrison, R.; Phillips, B.; White, T. L.; DiMare, M.; Rickborn, B. Unusual stability of N-methylmaleimide cycloadducts: characterization of isobenzofuran retro-Diels-Alder reactions. *J. Org. Chem.* **1993**, *58*, 6701−6706.
(35) Hoffmann, R.; Woodward, R. B. Orbital symmetry control of chemical reactions. *Science* **1970**, *167*, 825−831.
(36) Woodward, R. B.; Hoffmann, R. Stereochemistry of Electrocyclic Reactions. *J. Am. Chem. Soc.* **1965**, *87*, 395−397.
(37) Kumar, I.; Rana, S.; Cho, J. W. Cycloaddition reactions: a controlled approach for carbon nanotube functionalization. *Chemistry* **2011**, *17*, 11092−11101.
(38) He, X.; Kevlishvili, I.; Murcek, K.; Liu, P.; Star, A. [2pi + 2pi] Photocycloaddition of Enones to Single-Walled Carbon Nanotubes Creates Fluorescent Quantum Defects. *ACS Nano* **2021**, *15*, 4833−4844.
(39) Gifford, B. J.; Kilina, S.; Htoon, H.; Doorn, S. K.; Tretiak, S. Exciton Localization and Optical Emission in Aryl-Functionalized Carbon Nanotubes. *J. Phys. Chem. C* **2018**, *122*, 1828−1838.
(40) Wu, X.; Kim, M.; Qu, H.; Wang, Y. Single-defect spectroscopy in the shortwave infrared. *Nat. Commun.* **2019**, *10*, 2672.
(41) Qu, H.; Rayabharam, A.; Wu, X.; Wang, P.; Li, Y.; Fagan, J.; Aluru, N. R.; Wang, Y. Selective filling of n-hexane in a tight nanopore. *Nat. Commun.* **2021**, *12*, 310.
(42) Cambre, S.; Santos, S. M.; Wenseleers, W.; Nugraha, A. R.; Saito, R.; Cognet, L.; Lounis, B. Luminescence properties of individual empty and water-filled single-walled carbon nanotubes. *ACS Nano* **2012**, *6*, 2649−2655.
(43) Fagan, J. A.; Huh, J. Y.; Simpson, J. R.; Blackburn, J. L.; Holt, J. M.; Larsen, B. A.; Walker, A. R. Separation of empty and water-filled single-wall carbon nanotubes. *ACS Nano* **2011**, *5*, 3943−3953.
(44) Kim, M.; Adamska, L.; Hartmann, N. F.; Kwon, H.; Liu, J.; Velizhanin, K. A.; Piao, Y.; Powell, L. R.; Meany, B.; Doorn, S. K.; Tretiak, S.; Wang, Y. Fluorescent Carbon Nanotube Defects Manifest Substantial Vibrational Reorganization. *J. Phys. Chem. C* **2016**, *120*, 11268−11276.
(45) Frisch, M. J.; Trucks, G. W.; Schlegel, H. B.; Scuseria, G. E.; Robb, M. A.; Cheeseman, J. R.; Scalmani, G.; Barone, V.; Petersson, G. A.; Nakatsuji, H.; Li, X.; Caricato, M.; Marenich, A. V.; Bloino, J.; Janesko, B. G.; Gomperts, R.; Mennucci, B.;et al.: *Gaussian 09*. Gaussian, Inc.: Wallingford, CT, 2009.
(46) Yanai, T.; Tew, D. P.; Handy, N. C. A new hybrid exchange−correlation functional using the Coulomb-attenuating method (CAM-B3LYP). *Chem. Phys. Lett.* **2004**, *393*, 51−57.

https://doi.org/10.1021/jacs.4c08105
J. Am. Chem. Soc. 2024, 146, 23582−23590

(47) Binkley, J. S.; Pople, J. A.; Hehre, W. J. Self-consistent molecular orbital methods. 21. Small split-valence basis sets for first-row elements. *J. Am. Chem. Soc.* **1980**, *102*, 939−947.
(48) Martin, R. L. Natural transition orbitals. *J. Chem. Phys.* **2003**, *118*, 4775−4777.
(49) Gifford, B. J.; Sifain, A. E.; Htoon, H.; Doorn, S. K.; Kilina, S.; Tretiak, S. Correction Scheme for Comparison of Computed and Experimental Optical Transition Energies in Functionalized Single-Walled Carbon Nanotubes. *J. Phys. Chem. Lett.* **2018**, *9*, 2460−2468.
(50) Henkelman, G.; Uberuaga, B. P.; Jónsson, H. A climbing image nudged elastic band method for finding saddle points and minimum energy paths. *J. Chem. Phys.* **2000**, *113*, 9901−9904.
(51) Henkelman, G.; Jónsson, H. Improved tangent estimate in the nudged elastic band method for finding minimum energy paths and saddle points. *J. Chem. Phys.* **2000**, *113*, 9978−9985.
(52) Kresse, G.; Furthmüller, J. Efficient iterative schemes for ab initio total-energy calculations using a plane-wave basis set. *Phys. Rev. B* **1996**, *54*, 11169−11186.
(53) Perdew, J. P.; Burke, K.; Ernzerhof, M. Generalized Gradient Approximation Made Simple. *Phys. Rev. Lett.* **1997**, *78*, 1396−1396. [Phys. Rev. Lett. 77, 3865 (1996)].
(54) Kresse, G.; Joubert, D. From ultrasoft pseudopotentials to the projector augmented-wave method. *Phys. Rev. B* **1999**, *59*, 1758−1775.
(55) Dresselhaus, M. S.; Dresselhaus, G.; Saito, R.; Jorio, A. Raman spectroscopy of carbon nanotubes. *Phys. Rep.* **2005**, *409*, 47−99.
(56) Li, Y.; Wu, X.; Kim, M.; Fortner, J.; Qu, H.; Wang, Y. Fluorescent Ultrashort Nanotubes from Defect-Induced Chemical Cutting. *Chem. Mater.* **2019**, *31*, 4536−4544.
(57) He, X.; Sun, L.; Gifford, B. J.; Tretiak, S.; Piryatinski, A.; Li, X.; Htoon, H.; Doorn, S. K. Intrinsic limits of defect-state photoluminescence dynamics in functionalized carbon nanotubes. *Nanoscale* **2019**, *11*, 9125−9132.

https://doi.org/10.1021/jacs.4c08105
J. Am. Chem. Soc. 2024, 146, 23582−23590